State of Temperature Detection of Li-Ion Batteries by Intelligent Gray Box Model

Sudnya Vaidya*[a], Daniel Depernet [a], Salah Laghrouche [a], Daniela Chrenko [a]
[a] UTBM, CNRS, Institute FEMTO-ST, F-90000 Belfort, France
*sudnya.vaidya@utbm.fr

Abstract

Li-Ion batteries are among the key enablers of more sustainable use of energy. However, they need to be supervised and undergo continuous maintenance to assure safety and longevity. This paper focuses on the sensorless detection of the State of Temperature (SOT) of the Li-ion batteries during the operational life cycle of the battery irrespective of its state of charge. The paper presents the new Intelligent Gray Box Model (IGBM) to detect the SOT of Li-ion cells: that combines the three most powerful diagnostic tools Electrochemical Impedance Spectroscopy (EIS), Equivalent Circuit Model (ECM), and Artificial Neural Network Classifier (NNC). The work introduces the experimental test bench capable of emulating real-world and embedded constraints to conduct EIS onboard, its data preprocessing, and useful information extraction for the entire frequency spectrum. Furthermore, this paper presents a new hybrid parameter identification that combines the Whale Optimization Algorithm (WOA) and Levenberg Marquardt algorithm (LM) to identify the fractional order ECM. Finally, a neural network classifier is designed, optimized, and compared with different feature scaling techniques to evaluate its accuracy and robustness to detect and classify exact battery temperatures in real time from experimental data.

Keywords

Electrochemical Impedance Spectroscopy (EIS); Intelligent Gray Box Model (IGBM); Neural Network Classifiers (NNC); State of Charge (SOC); State of Temperature (SOT); Equivalent Circuit Model (ECM).

1. Introduction

The green energy transition has highlighted the interest in researching alternative energy storage systems, Li-ion batteries dominate the market due to their high energy efficiency. As a result, multiple electric propulsion systems are opting for the use of Li-ion batteries for their improved energy density, safety, and prolonged lifecycles. Often in applications such as the automotive industry, the Li-ion batteries are designed at optimized performance limits to reduce the cost associated with Electric Vehicles (EVs). In real-life operations the conditions of the battery vary continuously and can reach extreme conditions, not suitable to meet its predefined lifecycle duration [1]. Factors such as temperature, rate of charge, and discharge cause the battery to accelerate its degradation and produce faulty behavior quickly. Hence, the need for continuous battery cell monitoring to determine its characteristics over the various operating cycles is of prime concern to optimize its primary life and redefine the secondary life of batteries. One such method, widely used, is the measurement of the internal electrical impedance of the battery cell which can identify parameters such as the state of health, charge, and temperature of the battery [2]. Various studies using EIS have been carried out in the laboratory environment to benchmark the characteristics of battery cells. However, the major constraint remains the same, these techniques are limited to laboratory applications.

The optimal operation of batteries requires continuous monitoring of the quantities of stored and storable energy as well as a good assessment of the state of aging and the ability to meet the performance required by the application [3]. The current methods for temperature measurement require a large number of sensors, resulting in difficulty of organizing, servicing and maintenance using this large amount of data. Moreover, the estimation of the states of charge and health of batteries in operation gives limited results involving drifts, leading to reductions in energy performance [4-6].

1.1. Classical Fault Detection and Management for Li-batteries

Fault detection is critical and of prime importance in the operational lifecycle of Li-ion batteries, and in general for the safety of the user. Battery characteristics tend to be sensitive to the ambient temperature around them and are infamous for their thermal runaway and fire hazards [7]. An unmonitored excessive heating of the battery leads to its permanent destruction. The faults occurring inside a battery pack are usually inherited by individual cells. Hence individual battery cell monitoring techniques are being developed to detect defects, improper loads, hotspots of temperature, and harsh operational conditions and alert the Battery Thermal Management Systems (BTMS) to isolate and protect the battery units. Table 1 represents the faults occurring at cell level in a module of a battery pack. Faults occurring inside Li battery packs can be classified into various types depending on the source of the faults i.e., sensor-related [8], mechanical stress-related faults, or misread-miscalculated faults such as unequal current and voltage loads from BMS leading to overcharging and undercharging of cells [9-10], localized heating of the cells which leads to faster capacity fading of the cells individually in a pack.

Table 1: Cell level fault types.

Faults		
Short Circuits	(1)	Internal
	(2)	External
SOH	(1)	Capacity fade
	(2)	Rapid SEI growth
	(3)	Increased internal resistance
SOC	(1)	Overcharge
	(2)	Under charge
SOT	(1)	Cell overheating
	(2)	Thermal runaway
	(3)	Low temperature, Capacity fade

The temperature variation has a significant impact on the electrochemical processes of lithium-ion batteries, affecting their kinetic and thermodynamic properties [11]. The conductivity of the electrolyte affects the rate of solvation and desolvation of ions, which naturally increases the resistances involved in the charge and mass transfer processes. This relationship is often represented by Butler-Volmer equations and analyzed by the Arrhenius relation [12]. In this work, a temperature indicator is introduced, as State of Temperature (SOT) which indicates the internal temperature of the battery T_{bat}, as the intrinsic function of Electrochemical Impedance Spectroscopy (EIS) measured over a wide range of frequencies. SOT is mathematically expressed as Eq. (1)

$$SOT\ °C = EIS\ f\left[T_{bat} \pm \left(\frac{T_{bat} + \Delta T_{bat}}{T_{amb}}\right)\right] \tag{1}$$

Where, $\Delta T_{bat} \leq \pm 1°C$ accounts for the error in measurement, radial and longitudinal temperature variations across the battery surface. T_{amb} is the enforced operating temperature by the thermal chamber on the battery surface, assuming $T_{bat} = T_{amb}$ at thermal equilibrium and zero current. The presented work focuses on the detection of the SOT, including the SOC variations of the battery using the novel developed IGBM model.

1.2. Diagnostic Methods

The interplay between SOC, SOH, and SOT remains less explored for fault detection and diagnosis, most of the literature is based on the use of direct measurements followed by equivalent model parameter identification using Kalman filters [13]. The grey box models to indicate a relationship between EIS response and ECM were first proposed by Westerhoff et al. [14]. Gao et al. [15] presented a method to predict battery life using the relationship between EIS and ECM parameters. Several studies in literature follow a similar line of thought to estimate SOC and SOH of the battery [16-23]. Similarly, an equivalent circuit considering the internal temperature gradient was introduced by Jiang et al. [24], Zhang et al. [25], and Zhu et al. [26]. It presents the empirical dependence between ECM parameters and the temperature of the battery. Another approach includes numerical and mathematical models [9, 27-30]. Damay et al. [31] and Inui et al. [32] proposes a method based on Butler-Volmer and Arrhenius equations, which optimizes the surface resistance of the battery to detect its temperature. However, this method yields excellent results at positive

temperatures, but it performs poorly to detect negative temperatures of the cell. With the advance and flexibility of deep learning methods, many black box models use measurements directly from the battery to predict its states. Yang et al. [33] used a back-propagation regression neural network to predict the SOH of the battery with an error range of 6-10% in estimation. Tong et al. [34] used Long Short Term Memory (LSTM) and hybrid ensemble learning to predict capacity fading over cycles, the study reports 0.2-1% of Mean Square Error (MSE) for different battery chemistry. While Ma et al. [35] proposed a multi-fault diagnosis method for Li-ion battery pack using Principal Component Analysis (PCA) to reconstruct the fault waveforms (ohmic resistance, OCV, and voltage across the battery from the experimental data.

This article addresses the gap in the research by detecting the SOT of the battery cell, while the battery is still in service, irrespective of its SOC, and considering that the SOH remains constant during the experiment. Most of the literature on temperature detection of Li-ion batteries is based on the use of onboard thermal sensors, generating experimental data, making the diagnosis of SOT is often expensive and complex to manage for a battery pack. The method proposed in this paper provides a resilient method to classify battery cells at different temperatures robustly based on their impedance values using the NNC. The training of the network is done by using optimized equivalent circuit parameters which act as predefined strong input features. The ability to classify the SOT of batteries correctly, once the model is trained for a specific chemistry and cell type, provides an opportunity to implant the algorithm on onboard controllers, which can conduct EIS and later classify using the NNC.

Table 2: State of Art in Battery Diagnosis.

Study	Diagnosis Technique	Cell Type	Fault Classification	Characteristics	Reference
Diego et al. (2022)	ECM Electro-thermal model using constrained Zonotopes	NA Simulation,	Resistance Estimation -Incorrect Cooling -Internal Thermal -Core Temperature Rise	(1) Purely mathematical model (2) Uses set-based Estimation. (3) 30-45% Estimation error in predicting three resistances	[9]
Zhang et al. (2022)	Laboratory EIS, Equivalent Circuit	LiCoO2 NCM NCA	State of Charge (SOC) The link between ECM and EIS	(1) Simulated annealing Optimization. (2) MAE 2.6% (3) Offline	[25]
Zhu et al. (2015)	Laboratory EIS +ECM	Commercial Suzhou Phylion 8 Ah	-Internal Temperature and SOC	(1) Online Lookup table (2) Based on the Phase Shift of impedance to detect SOT, SOC (3) The method is redundant due to the few selected frequencies. (4) MAE Error 8%	[26]
Zongxiang et al. (2022)	Weighted Pearson Coefficient, Sparse Data Observer Voltage, Current measurements	Li-ion	Short circuit and sensor Faults	(1) Offline (2) Highly Sensitive to forgetting parameters. (3) Error % not reported.	[28]
Damay et al. (2021)	Laboratory EIS + ECM, GITT	Commercial LiFePO4, 40 Ah	-Internal temperature -Fixed SOC	(1) Based on Butler Volmer and Arrhenius Equation. (2) Contribution of the amplitude of the excitation pulse and temperature. (3) Low accuracy at lower temperatures	[31]
Inui et al. (2021)	Laboratory EIS + ECM	Samsung: ICR18650-22F, Sony: US18650GR NMC, 2.2 Ah	-Internal temperature - Fixed SOC	(1) Based on Arrhenius Equation. (2) Strongly dependent on estimation of activation energy (3) No information for lower Temperatures (+10 to + 40°C)	[32]
Yang et al. (2017)	HPPC Test + ECM+ Neural Network	LiFePO4	-State of Health SOH Estimation	(1) Offline (2) Simple first-order ECM. (3) MAE Error 8%	[33]
Ma et al. (2022)	PCA Fault waveform reconstruction Terminal Voltage, OCV, ohmic resistance	Li -ion	Connection faults and External Short circuit	(1) Online (2) Highly Sensitive to Input Ohmic resistance and OCV, Voltage (3) Error % not reported	[35]

2. Novel Gray Box Methodology

The proposed method in Fig. 1 depicts the novel Intelligent Gray Box Model (IGBM) that aims to develop an embedded integrated monitoring system which is capable of determining SOC, SOH, and SOT on a real-time basis for the onboard diagnosis system. The inspiration for this approach stems from studying and addressing the limitations observed in the individual methods documented in Table 2 of the literature. For instance, relying solely on EIS is susceptible to the specific frequency range chosen for establishing correlations between the SOC, SOH, SOT, and the operational condition of the cell. This limitation can result in less robust identification of the causes of faults. However, the gray box model addresses these shortcomings by combining the simplicity of EIS with hybrid optimized equivalent circuit parameter identification. Which then extracts the features (ECM parameters) from the entire EIS spectrum rather than only depending on several interesting frequency points. The extracted features are fed as input to a NNC to identify the SOT. The main advantage of this methodology is that the noises and stochastic errors of EIS measurements under different frequencies can be counteracted and thus retain more useful information between different input features and the predicted output. The method provides a possibility of transferring the learning of the model on an embedded controller for onboard applications, thus enabling a real-time online embedded diagnosis method.

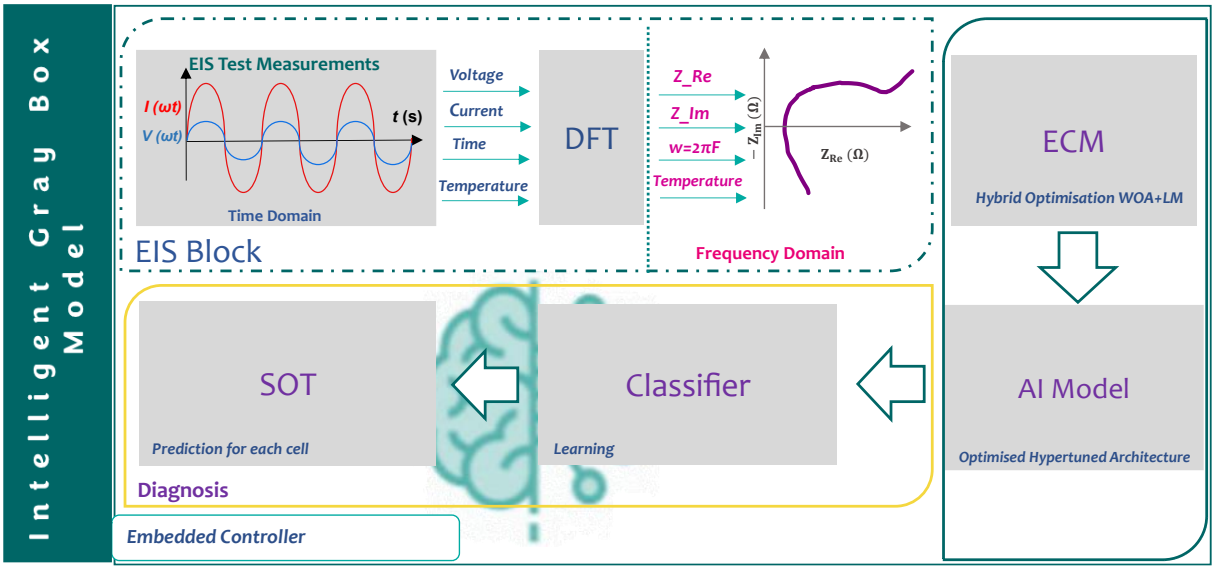

Figure 1: Intelligent Gray Box Model

The principle of the presented IGBM is adaptable to different chemistries of Li-ion batteries, and other electrochemical energy storage systems like fuel cells, Na batteries, etc. and can hence, be used to predict the exact value of SOH, and or Remaining Useful Life (RUL), SOC and SOT of batteries.

2.1. Electrochemical Impedance Spectroscopy

Batteries are often subjected to fast dynamic changes to meet up the load demands, multiple slow and fast processes occur inside the battery while it's in operation. These phenomena tend to interfere with each other and create complex behavior [36]. EIS is a non-destructive technique used to study the dynamic response of the battery by subjecting it to a small excitation current signal $I_{(\omega t)}$ and measuring its response voltage $V_{(\omega t)}$signal (by galvanostatic method). Eq. (2) represents the impedance calculated from the current and voltage signals of the battery.

$$Z = \frac{\overrightarrow{V_{(\omega)}}}{\overrightarrow{I_{(\omega)}}} = \frac{\hat{V} - OCV}{\hat{I}} = Z_{re}(\omega) + j.Z_{Im}(\omega) \tag{2}$$

2.2. Equivalent Circuit of Li-Ion Battery Cell

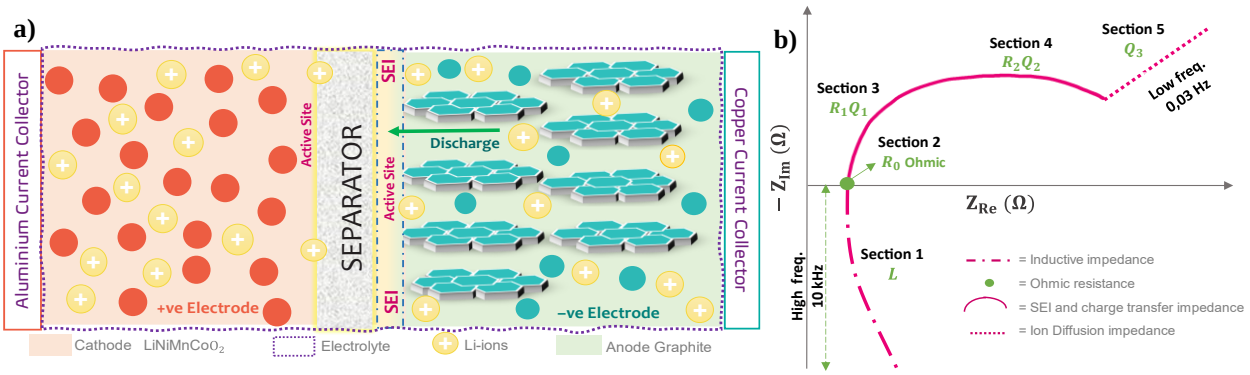

Figure 2: General layouts for Li-ion batteries (a) internal structure of NMC (b) physical link between ECM and EIS.

Equivalent circuit parameters are used to associate the physical effects occurring inside the electrochemical system, i.e., the battery cell. Fig. 2(a) presents the general structure of the Li-batteries where the positive electrode is made of the battery technology definition here Nickel Manganese Cobalt Oxide (NMC 111) cathode with 33% concentration each and the anode is made up of graphite [37]. As the battery ages, it tends to lose its capacity due to the rapid increase of the Solid Electrolyte Interphase (SEI), a layer that is developed by multiple charge and discharge cycles [24, 31]. It increases the resistance faced by ions in porous transfer, at the active site between the separator membranes. This impedance is represented in the frequential domain on the Nyquist plot as a semi-arc in Section 3 of Fig. 2(b) Similarly, Section 1 represents the inductive effects caused by the movement of electrons in the wire and winding of internal electrodes. Section 2 represents the initial internal electric and ionic resistance encountered by the current collectors, active materials, electrolyte, and the separator within the battery. Following Section 4 showcases the charge transfer resistance experienced by ions [38]. Various equivalent circuits are presented in the literature describing thermal, electric, and kinetic models. In reality, these are complex phenomena occurring at different time constants and the use of RC grid circuits ceases to be accurate. Eq. (3) describes a Constant Phase Element (CPE) that fine-tunes the fitting results by providing fractional order models to rectify the time constants.

$$Z_{CPE} = \frac{1}{Q(j\omega)^{\phi}} \tag{3}$$

where Q is the generalized capacitance and ϕ is the power depression factor. In parallel with resistance, CPE acts as a ZARC element, it is purely resistive when ϕ is 0 and it's a pure capacitor when ϕ =1. Section 5 represents the slower process of three different diffusions occurring inside the battery cell, namely the diffusion of lithium atoms in the active materials of both electrodes and the diffusion of lithium ions in the electrolyte [38, 39]. Traditionally it is represented by the Warburg element of finite length or finite space. However, in this study, we found using CPE element with variable power ϕ to represent the semi-infinite diffusion process as a function of the temperature of the battery to be more coherent. Thus, the above model expresses the relationship between ECM parameters and the electrochemical, thermal, and kinetic phenomenon of the battery.

3. Experimental Setup

The interest of developing this particular methodology of conducting EIS using an electronic load is to understand and be able to control and emulate all the constraints faced in an embedded environment, such as controlling the frequency of sampling and emulating the current profiles coherent to real-world driving cycles. The developed test bench presented in Fig. 3(a) and Fig. 3(b) is capable of rapid charge and discharge cycles, implementing accelerated capacity fading due to extreme temperature conditions, etc. All the operating conditions that might arise in the actual real world can be programmed and defined using the developed Human-Machine Interface in LabVIEW.

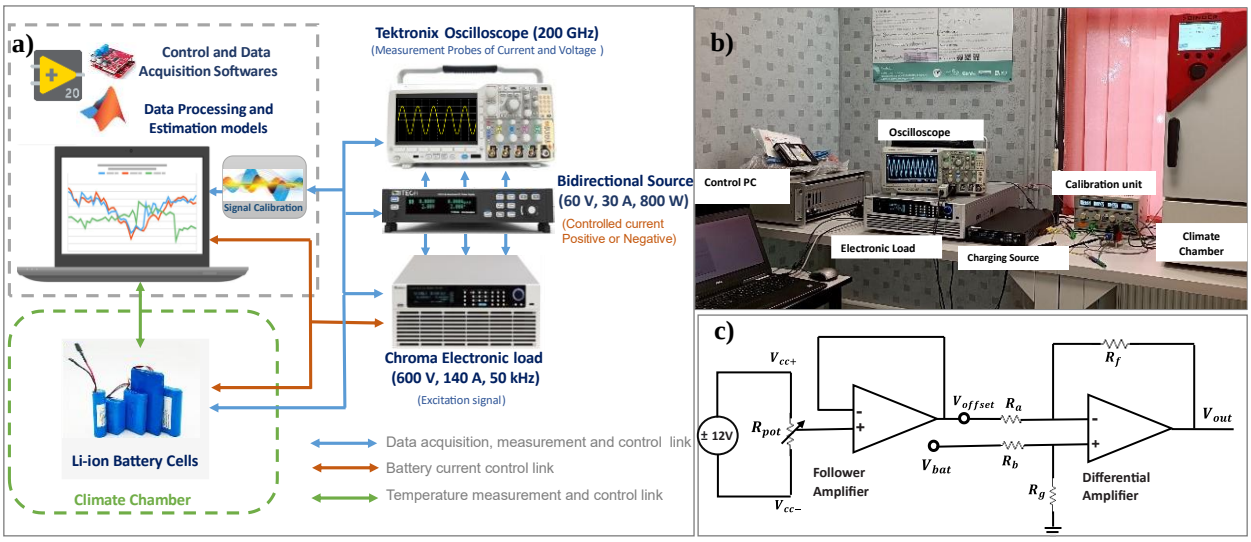

Figure 3: Experimental Test Bench (a) designed EIS set up (b)actual test bench (c) calibration unit.

3.1 Data Acquisition and Processing

The electronic load Chroma brand 63202A series, 600 V, 140 A, and the power source ITECH M3432, 60 V, 30 A are connected in parallel to allow charging and discharging regulation of the DC and AC components of the current in the battery, supplied by the user. The amplitude of the excitation signal is always kept below the nominal battery current to respect the linear domain of the model and validate the EIS readings. For precise data acquisition of signals, an oscilloscope of Tektronix model MDO3024 200 GHz is connected by its current and voltage probes across the circuit to measure the signals. Data signals for fixed 10,000 samples are recorded at each frequency of EIS measurement. National Instruments LabView 21 Virtual Instrument Software Architecture (VISA) was created to control, automate, and acquire the signal data.

Fig. 3(c) illustrates the calibration unit which utilizes a printed circuit board based on a differential operational amplifier to enhance the signal-to-noise ratio. The board incorporates known resistances for both calibration and amplification of the sinusoidal battery voltage response. Then the amplified signal V_{out} can be defined by Eq. (4) where V_{bat} is the cell voltage, V_{offset} the voltage set to OCV and gain the amplification rate of the sinusoidal component of V_{bat}.

$$V_{out} = gain\left(V_{bat} - V_{offset}\right) \tag{4}$$

3.1.1 Preprocessing from Time to Frequential Domain

The voltage and current signals acquired from the oscilloscope are in the time domain such that for each frequency point of measurement is recorded with their discrete time interval between samples, this discrete time is predefined and controlled by adjusting the number of periods k of the signal and its sampling frequency F_s at which the data is acquired. The N samples of a signal allow the real and imaginary parts of harmonics of rank k to be computed. The rank of the corresponding harmonic to the excitation is defined as the number of measurement periods. The computation of current excitation $I_{(\omega t)}$ and its voltage response $V_{(\omega t)}$ in the frequency domain is carried out using Eqs. (5) and (6) of the Discrete Fourier Transform (DFT) as presented in the algorithm. (1), from the previous works of Depernet et al [40]. The computation of impedance at that frequency of excitation is computed by Eq. (7). The DFT function is described in the algorithm. (1), it performs an iteration over the number of frequency points set (ω), to store real Z_{Re} and imaginary Z_{Im} impedance values of the battery cell, the data is saved as a .mat file for that measurement and SOC level.

Algorithm 1: Discrete Fourier Transformation

Input: Load the directory and path of data files
Define ω (10000, 9000, ...,0.03 Hz)
for soc ∈= {(0,1,2,3,..7)} %No.of SOC levels of cell do
  for i ∈= $\{0, \ldots., \omega(N_f)\}$ %No.frequencies of EIS do
    Import data files, I, V, k, n, N, dt (sampling time interval)
    Perform DFT of V, I (Eq. 5, 6)
    Calculate Real and imaginary parts of V, I for each harmonic rank n, k.

$$\begin{Bmatrix} I_{Re}(f) = \frac{2}{N}\sum_{n=0}^{N-1} I(n) * \cos\left(\frac{2\pi kn}{N}\right) \\ I_{Im}(f) = -\frac{2}{N}\sum_{n=0}^{N-1} I(n) * \sin\left(\frac{2\pi kn}{N}\right) \end{Bmatrix} \quad (5)$$

$$\begin{Bmatrix} V_{Re}(f) = \frac{2}{N}\sum_{n=0}^{N-1} V(n) * \cos\left(\frac{2\pi kn}{N}\right) \\ V_{Im}(f) = -\frac{2}{N}\sum_{n=0}^{N-1} V(n) * \sin\left(\frac{2\pi kn}{N}\right) \end{Bmatrix} \quad (6)$$

    Calculate Impedance values Z_{Re} , Z_{Im} using Eq. (7)

$$\begin{Bmatrix} Z_{Re} = \frac{(V_{Re})*(I_{Re})+(V_{Im})*(I_{Im})}{(I_{Re})^2+(I_{Im})^2} \\ Z_{Im} = \frac{(I_{Re})*(V_{Im})-(V_{Re})*(I_{Im})}{(I_{Re})^2+(I_{Im})^2} \end{Bmatrix} \quad (7)$$

    Store Z_{Re} , Z_{Im} and ω
  end
  soc+=1 % move to next soc EIS readings
end

3.1.2 Validation of Experimental Test Bench

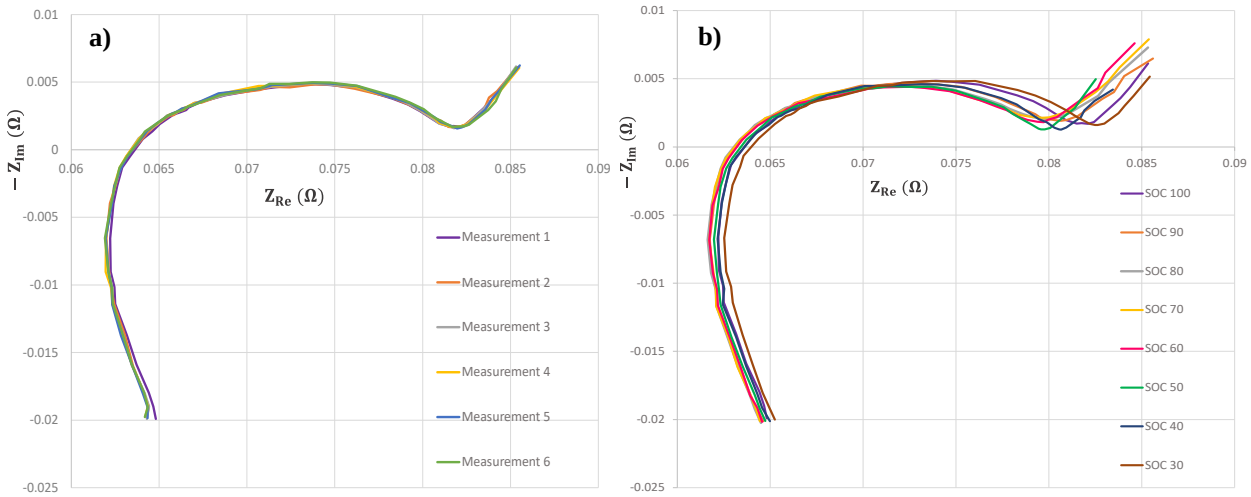

Figure 4: EIS of the cell (a) repeatability of the set-up SOC 100%, 25 °C (b) different SOC of the cell, 25 °C.

EIS setup in general tends to be very sensitive with respect to the connecting cables, the parasitic inductance of the apparatus used, the external influence of temperature or voltage flux deviation from the source, etc. Validation of the developed test bench was carried out by conducting a set of 6 consecutive EIS under similar operating conditions for the same cell and the results are compared are shown in Fig. 4(a), EIS is measured with the direct current I_{dc} equal to 0 A and excitation I_{ac} equal to 0.5 A maintaining the battery cell at 25°C and fully charged at SOC100% with 5 minutes of rest time between each EIS. The Nyquist plot of the first EIS test is identical to the other five consecutive readings proving the robustness and fidelity of the setup to capture the same response at each repetition of the test, under similar conditions.

$$SOC = \frac{C_{Instantaneous}}{C_{Nominal}} * 100\% \quad (8)$$

$$C_{Instantaneous} = \int_{t_0}^{t_1} I(t) * dt \quad (9)$$

Eq. (8) describes the SOC indicator measuring the instantaneous capacity $C_{Instantaneous}$ of the battery to the rated maximum capacity $C_{Nominal}$ of the battery, where the instantaneous capacity is calculated by Eq. (9) and t_0 = 0 s, t_1 = 720 s for I_{dc} = 1.3 A discharge current.

3.2 Tests to Characterize Battery SOC and SOT

The tests are conducted using a Samsung ICR18650-26F cylindrical cell, with cathode composition as NMC111, 3.7 V nominal voltage, and 2600 mAh nominal capacity, cut-off voltage is specified by the manufacturer as 2.75 V and an initial AC impedance of equal or less than 100 mΩ at 1kHz. The battery cell is supposed to last 299 standard CC-CV cycles [37]. The battery cell under tests has prior 2 years of calendar aging, it was stored in appropriate dry and stable thermal conditions at 25°C with none of the none of the cyclic aging. The entire test campaign of 480 tests was conducted in 2 consecutive weeks to avoid any SOH variation. Table 3 describes the test campaign that was designed with the help of the LabVIEW based test bench supervision to conduct 6 consecutive EIS at each SOC level while controlling the temperature of the climate chamber. Four hours of rest in the set temperature of the climate chamber is respected before launching the EIS tests to achieve a uniform battery surface temperature (T_{bat}) and thermal equilibrium, which is monitored using two temperature sensors (Pt-100 and k-type thermocouple) placed centrally on the top of the surface of the cell throughout the test. Heating of the battery cell due to discharging, and excitation accounts for a ΔT_{bat} of less than 0.1°C. Between each discharge of 10% SOC a rest time of 30 minutes is incorporated to achieve electrochemical equilibrium and to account for the OCV stabilization of the battery post-charge and discharge. Fig. 4(b) represents the first measurement of EIS at subsequent SOC levels between 100-30%.

Table 3: EIS Test Campaign.

Steps	Process	Units
1	Charge Cell CC-CV	1.3 A, 3 h till 4.2 V
	Rest	24 h
2	Set the Temperature of the cell in the thermal Chamber	4 h Before test
3	Measure OCV, Calculate SOC	Instantaneous before Test
4	6 EIS tests at $SOC_{initial}$=100%, fully charged cell	I_{dc} =0 A, I_{ac} =0.5 A, 0.03 Hz-10 kHz
5	Discharge cell CC by 10% of $SOC_{initial}$	1.3 A, 0.5 C for 720 seconds
6	Rest	1800 seconds
7	6 EIS tests $(SOC_{initial} - 10)\%$	I_{dc} =0 A, I_{ac} =0.5A, 0.03 Hz-10 kHz
	Repeat (the steps 5,6,7 until SOC drops to 30%)	
8	Repeat the procedure for all Temperatures	T_{amb} = [-10, -5,0,5,10,15,20,25,30,35] °C

4 Hybrid Estimation of Equivalent Circuit Parameters

Parameter identification aims to find the value of the unknown ideally optimized parameter vector θ of the equivalent circuit model so that the identified model represents the experimental values as closely as possible [41]. Since the Nyquist plot represents both real and imaginary parts of impedance spectroscopy, essentially this becomes a minimization of the nonlinear least square problem as described in Eq. (10).

$$\left\{min_x\, F(x) = \sum_i^N \left\{\left(Z_{Re_{Exp}}(\omega) - Z_{Re_{model}}(\omega,\theta)\right)^2 + \left(Z_{Im_{Exp}}(\omega) - Z_{Im_{model}}(\omega,\theta)\right)^2\right\}\right. \quad (10)$$

Model parameters are calculated based on ECM described in Fig. 5(a), Eq. (11) shows the total impedance of the proposed ECM model which is replaced in Eq. (10).

$$Z_{model} = \left\{R_0 + L(j\omega) + \frac{R_1}{1 + R_1Q_1(j\omega)^{\phi_1}} + \frac{R_2}{1 + R_2Q_2(j\omega)^{\phi_2}} + \frac{1}{Q_3(j\omega)^{\phi_3}}\right\} \quad (11)$$

$$Z_{Re_{model}} = f\{R_0, R_1, R_2, Q_1, Q_2, Q_3, \phi_1, \phi_2, \phi_3, \omega\} \quad (12)$$

$$Z_{Im_{model}} = f\{R_0, \mathrm{L}, R_1, R_2, Q_1, Q_2, Q_3, \phi_1, \phi_2, \phi_3, \omega\} \quad (13)$$

The real and imaginary parts of impedance are calculated by splitting denominators using Euler's formula. The dependency of ECM parameters in the objective function is defined as follows in Eqs. (12) and (13) and can further be accessed in Appendix A of the supplementary material.

Thus, the estimation vector of the objective function has 10 parameters in Eq. (14)

$$\theta = f\{R_0, \mathrm{L}, R_1, R_2, Q_1, Q_2, Q_3, \phi_1, \phi_2, \phi_3, \omega\} \quad (14)$$

In most of the standard optimization processes, it is necessary to set appropriate initial conditions for the algorithm so that it can locate the global minimum and does not get stuck in a local minimum. To overcome this hurdle, we propose the hybrid optimization routine in Fig. 5(b), where the Whale Optimization Algorithm (WOA) acts as a global optimizer and pre-allocates a very close to true value initial guess ($\theta_{initial}$) and then local optimization is carried out using the Levenberg Marquardt (LM) algorithm which refines and estimates the final local minimum. The Root Mean Square Error (RMSE) and Mean Absolute Error (MAE) are used as the fitness evaluation metric. Mirjalili et al. [42], presented the WOA technique, it is a metaheuristic optimization algorithm inspired by the social behavior and hunting strategy of humpback whales in a group. The algorithm mimics the three phases of whales during their prey foraging search, encircle and attack to find the optimal solution. The number of search agents (whales) and the initial population is defined N, and the location of whales and potential solutions (location of prey) is updated at each iteration based on the probability function that favors exploration in high-dimensional space and potential of likely solutions found based on a fitting criterion.

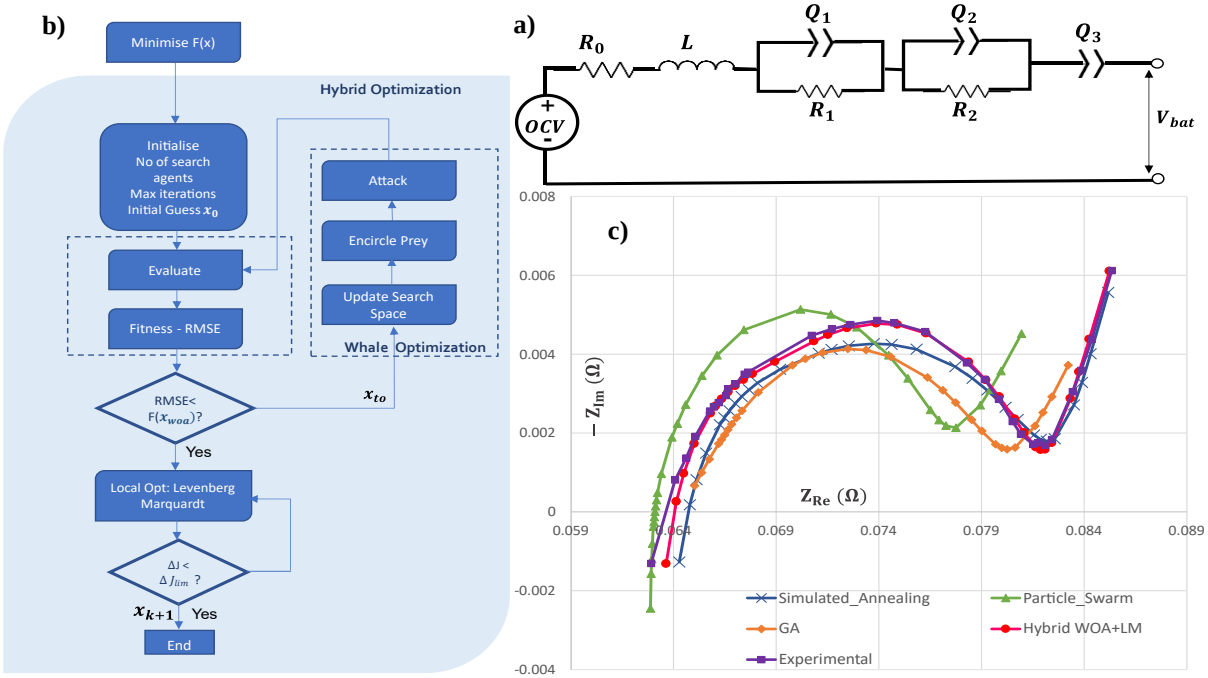

Figure 5: Hybrid Optimization (a)equivalent circuit Model of Li-ion cell (b)WOA and LM algorithm (c)comparison of various optimization techniques.

The LM method combines both the Gauss-Newton method and the gradient descent method, at each iteration it minimizes the objective function $min_x\, F(x)$ by approximating second-order Taylor expansion around x_k as the current estimate and new estimation at x_{k+1} represented in Eq. (15)

$$F(x) \approx F(x_k) + (x - x_k)^T J_k^T f_k + \frac{1}{2} * (x - x_k)^T J_k^T J_k (x - x_k) \quad (15)$$

where J_k is the Jacobian matrix of $F(x)$ evaluated at x_k, and f_k is the vector of residuals evaluated at x_k . To minimize the above approximation of $F(x)$ we set the gradient to zero, which yields $J_k^T J_k$ the Hessian unstable, as its positive definiteness cannot be ensured, to increase the stability and convergence. The LM algorithm uses scalar damping factor λ multiplied by the identity matrix such updated parameters p_k are given as in Eqs. (16) and (17):

$$(J_k^T J_k + \lambda_k * I) * p_k = -J_k^T f_k \quad (16)$$

$$(p_k = (J_k^T J_k + \lambda_k I)^{-1} J_k^T f_k) \quad (17)$$

The updated parameter vector is given as follows in Eq. (18):

$$x_{\{k+1\}} = x_k + p_k \quad (18)$$

To evaluate the effect of the proposed parameter identification method, several existing algorithms such as particle swarm optimization (PSO), genetic algorithm (GA), and simulated annealing algorithm (SAA) were implemented and evaluated based on a fixed number of iterations and means square error metrics. The results of the comparison between various optimization techniques are depicted in Fig. 5(c). Using EIS data of battery cell at 25°C and SOC100% from measurement 1, the identified results are compared in Table 4. It can be observed that the proposed WOA-LM algorithm has the smallest RMSE error of 0.0144 Ω as compared to the SAA, GA, and PSO methods. The obtained parameters show great variation between them, indicating how highly non-linear the objective function is; thus, a highly accurate parameter identification method is necessary.

Table 4: Comparison of Various Global Optimizers.

Method	R_0 (Ω)	L (µH)	R_1 (Ω)	Q_1 ($F.s^{(1-\phi_1)}$)	ϕ_1	R_2 (Ω)	Q_2 ($F.s^{(1-\phi_2)}$)	ϕ_2	Q_3 ($F.s^{(1-\phi_3)}$)	ϕ_3	RMSE (Ω)	Time (mins' s")
SAA	0.0627	0.32	0.0167	2.8501	0.5732	0.0033	0.1684	0.9200	558.8	0.7156	0.0146	4', 41.38"
PSO	0.0604	0.13	0.0147	2.5593	0.8524	0.0044	0.0391	0.6832	432.3	0.7016	0.0198	3', 19.27"
GA	0.0597	0.32	0.0156	2.1500	0.6116	0.0048	0.0120	0.9983	515.5	0.5386	0.0149	7', 53.06"
WOA-LM	0.0626	0.32	0.0152	1.6561	0.6878	0.0042	0.0670	0.9990	458.8	0.6837	0.0144	2', 39.54"

4.1. EIS Results and ECM Validation

4.1.1.EIS at different SOC of the battery cell

To obtain a maximum of information from a minimum of experiments, the influence of temperature at constant SOC and the influence of SOC at constant temperature were studied for 43 frequencies between 10 kHz to 0.03 Hz. The effect of different SOC levels at a fixed temperature is nearly insignificant in the high-frequency zone irrespective of the SOT of the battery. Fig. 6(a) depicts the results of fitting between ECM parameters using and EIS results at different SOC levels at -10°C. As we see the effect of temperature influences directly on the distinction of SOC levels in the middle-frequency zone, a clear separation is observed in the lower-frequency zone from 30 Hz – 5 Hz. The Warburg tail appears at very low frequencies 3 Hz - 0.03 Hz as temperature decreases the appearance of the tail is delayed because of the slow diffusion of ions owing to the lower temperatures, hence the lowest frequency limit (0.03 Hz) by EIS test bench has been adapted for all experiments. The fitting results are presented in Table 5.

Table 5: ECM Parameters at different SOC of the battery at -10°C SOT.

SOC%	R_0 (Ω)	L (H)	R_1 (Ω)	Q_1 ($F.s^{(1-\phi_1)}$)	ϕ_1	R_2 (Ω)	Q_2 ($F.s^{(1-\phi_2)}$)	ϕ_2	Q_3 ($F.s^{(1-\phi_3)}$)	ϕ_3	RMSE (Ω)
100	0.07180	3.3E-07	0.1398	2.0193	0.7912	0.1422	1.6004	0.4565	325.7283	0.8500	0.0648
90	0.07387	3.2E-07	0.2353	1.3744	0.5507	0.0081	0.1312	0.8555	323.0678	1.9378	0.0548
80	0.07354	3.2E-07	0.1842	1.3993	0.5298	0.0050	0.1390	0.8630	324.3784	0.9578	0.0428
70	0.07404	3.2E-07	0.1342	1.1247	0.6596	0.0195	0.4805	0.6539	321.9506	0.8914	0.0395
60	0.07449	3.2E-07	0.1405	1.0880	0.6561	0.0183	0.4043	0.6755	310.4991	0.7135	0.0392
50	0.07460	3.2E-07	0.1494	1.1597	0.6508	0.0207	0.5334	0.6355	589.5738	0.9178	0.0407
40	0.07295	3.2E-07	0.1365	1.1618	0.6727	0.0609	1.9056	0.4494	899.6827	1.0457	0.0450
30	0.07404	3.2E-07	0.0405	1.1806	0.9701	0.2209	1.7105	0.4630	1100.000	1.1267	0.0540

The ohmic resistance R_0 and inductance L are almost constant. Higher changes are observed on R_2 and Q_2 in the charge transfer globe, but the pattern remains highly nonlinear and complex due to the dominant effect of temperature, which can be explained due to slower chemical processes at low cell temperatures and corresponding higher cell impedance. Especially diffusion processes strongly depend on temperature, which is represented in Fick's law by the diffusion coefficient. The Warburg Q_3 parameter shows a distinct increase with a decrease in SOC representing slow diffusion. At low temperatures, an interesting effect on the diameter of the second semi-circle can be seen clearly. In Fig. 6(a), from 100 to 60% SOC, the diameter of the second semi-circle decreases with SOC but increases again at lower SOCs. This effect could be due to the specific chemistry of the cell. The results of our study remain synchronous with the findings of [32, 36].

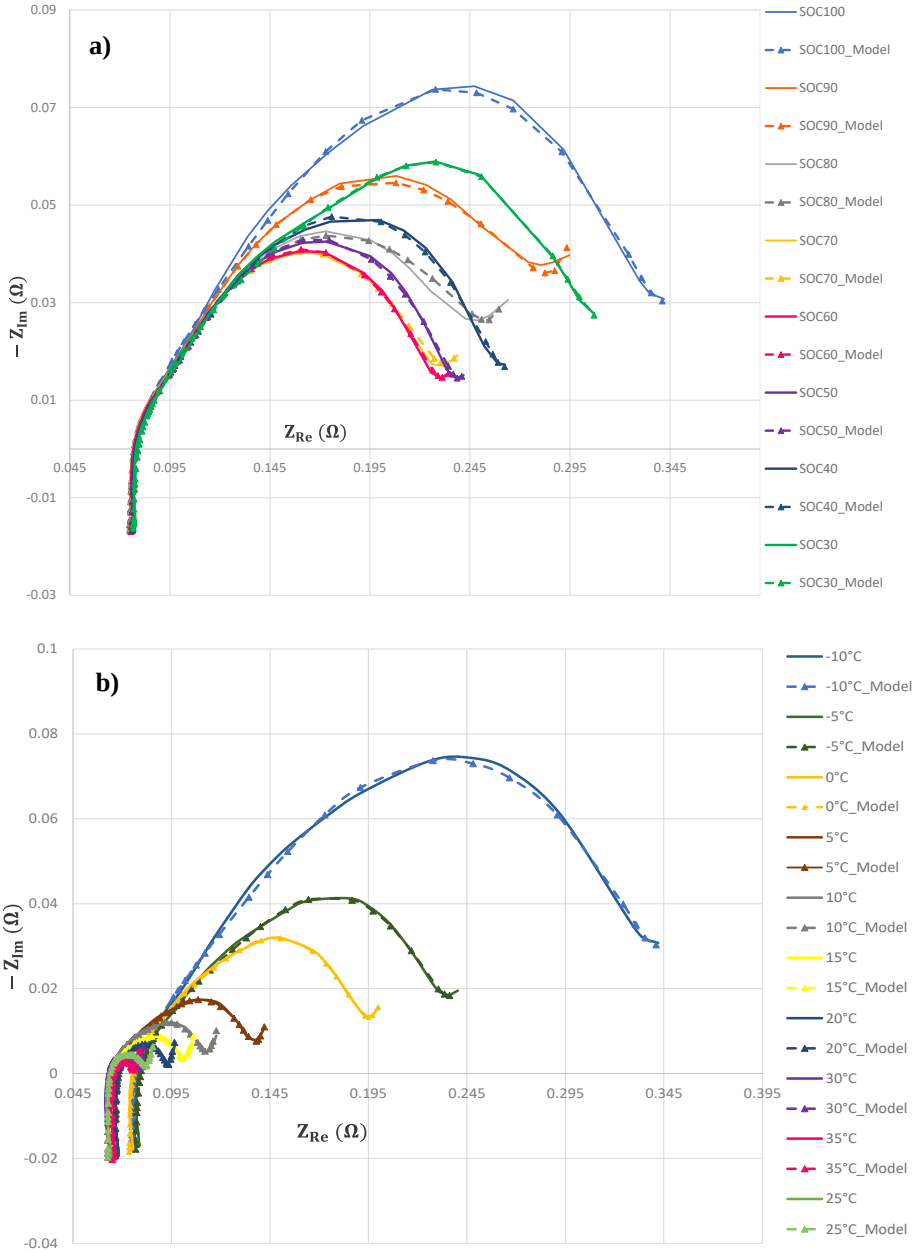

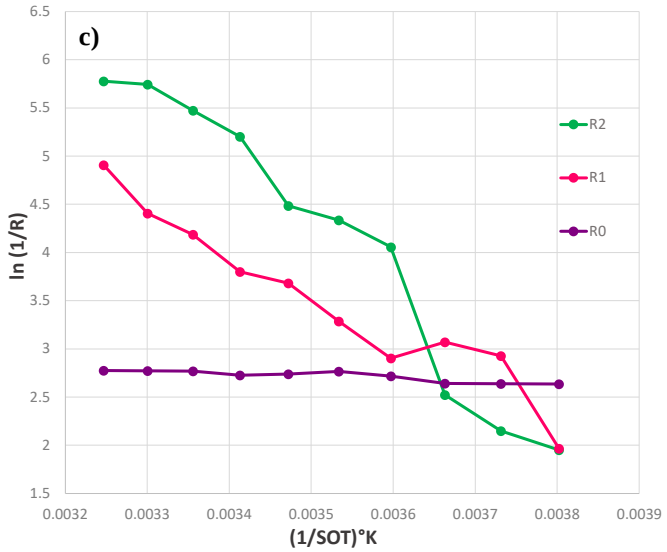

Figure 6: Optimized fitting curves between experimental EIS and ECM (a) different SOC, -10°C (b) different SOT, 100% SOC (c) Arrhenius plot for obtained ECM parameters.

4.1.2.EIS at different temperature of the battery cell

Thermal equilibrium is achieved by resting the battery cell in the thermal chamber at set SOT for 4 h. The influence of SOT was investigated at ten points for both positive and negative temperatures between (-10°C to +35°C) at fixed SOC levels. Two clear groups of the spectrum can be seen in Fig. 6(b), the smaller globes belonging to the higher temperature range (35°C to 5°C) and the latter representing lower temperature spectrums (0°C to -10°C). The developed ECM of the battery is capable of correctly co-relating to experimental EIS curves. There is a negligible effect observed in the higher frequency zone and the first globe of SEI. At lower temperatures, the lithium plating and dendrite formation occurs [43], further the thermal energy of ions decreases, lowering their kinetic energy. Hence, the ions move slower through the interphase and accordingly, the resistance gets higher. The same effect can be applied to explain the second circle which is a mix of charge transfer and diffusion processes. Again, both processes are functions of temperature, and the resistance is thus higher. The increase in R_0 at low temperatures is due to an increase in the viscosity of the electrolyte, and a reduction in its ionic conductivity. From 5°C to 20°C, the two globes are seen separately, as the temperature rises the globes cannot be distinguished. The Arrhenius plots of the resistances R_0, R_1 and R_2 are represented in Fig. 6(c) as function of temperature, since the plots are almost linear in nature from (0°C to 35°C) it allows to confirm the validity of the obtained ECM parameters [11,12].

Table 6: ECM Parameters at different SOT of the battery with constant SOC 100%.

SOT	R_0 (Ω)	L (H)	R_1 (Ω)	Q_1 ($F.s^{(1-\phi_1)}$)	ϕ_1	R_2 (Ω)	Q_2 ($F.s^{(1-\phi_2)}$)	ϕ_2	Q_3 ($F.s^{(1-\phi_3)}$)	ϕ_3	RMSE (Ω)
-10°C	0.07180	3.0E-07	0.1398	2.0193	0.7912	0.1422	1.6004	0.4565	325.7283	0.8500	0.0648
-5°C	0.07140	3.2E-07	0.0535	3.3439	0.8659	0.1165	1.6630	0.4619	300.2110	0.7733	0.0400
0°C	0.07125	3.3E-07	0.0464	2.8843	0.8461	0.0803	1.5973	0.4841	254.1951	0.7020	0.0322
5°C	0.06600	3.2E-07	0.0548	1.9499	0.6743	0.0173	0.3831	0.7162	295.5765	0.6859	0.0219
10°C	0.06286	3.3E-07	0.0374	2.0015	0.6739	0.0131	0.4168	0.7061	297.0441	0.6903	0.0183
15°C	0.06470	3.2E-07	0.0252	2.0007	0.6889	0.0113	0.4205	0.7238	297.0442	0.6429	0.0160
20°C	0.06555	3.2E-07	0.0224	1.3914	0.6741	0.0055	0.3362	0.7534	435.7201	0.7344	0.0150
25°C	0.06269	3.2E-07	0.0152	1.6561	0.6878	0.0042	0.0670	0.9990	458.8836	0.6837	0.0144
30°C	0.06258	3.2E-07	0.0122	1.5800	0.7182	0.0032	0.1478	0.9997	432.1879	0.6752	0.0143
35°C	0.06242	3.3E-07	0.0074	1.4942	0.7755	0.0031	0.0914	1.0000	439.6680	0.6236	0.0143

The effects at high temperatures are much more complex than those at low temperatures. High-temperature conditions accelerate thermal aging by rapid increase in SEI layer, decomposition of electrolyte and binder material which could explain the complex fusion of the two globes into one [43], further complicating the identification of a pattern or direct

link between ECM parameters and SOT. To overcome the problem of depending on the most promising parameters, develop an empirical relation between ECM parameters and SOT. A neural network model is implemented which learns this hidden pattern between datasets and calculates the weight matrix for us.

5. Artificial Neural Classifiers

Neural networks can be defined as function approximates; the idea is to estimate an unknown function using it to classify the outcome to which it could belong. In order to identify the unknown function, both the inputs and the outputs of the function are labeled, this kind of classifier is called a supervised classifier and the neural network problem becomes supervised. Supervised neural networks pertains to a set of known outcomes. However, when the true sets of labels or predefined outputs aren't provided then the errors are meaningless. This method is known as unsupervised learning.

The goal of the NNC is to categorize temperature clusters within the ECM dataset obtained from experimental values, as outlined in Table 5 and Table 6, for each specific SOT measurement. Fig. 7(a) outlines the general steps followed by IGBM in SOT diagnosis.

5.1 Data for AI model

The biggest advantage of the proposed IGBM is the input data that it uses to implement Machine Learning. Many studies report using direct experimental signals to train a neural network, or they are based on statistical data analysis of ECM parameters [44]. In this study, we use the obtained parameters from the hybrid WOA-LM optimization method with fixed criteria of RMSE lower than 0.01Ω for all the experimental EIS tests i.e., 480 data sets at ten different SOT and eight different discharged SOC levels, six repetitive EIS are conducted at each point. Appendix B exhibits a detailed representation of all the ECM data as a pair plot used as an input to train the network. A pair plot visualizes the data to find the relationship between them where the variables can be continuous or categorical. It is used to understand the best set of features to explain a relationship between two variables or to form the most separated clusters. It also helps to form some simple classification models by drawing some simple lines or making linear separations in our dataset, for example by Support Vector Classifiers (SVC). Since the ECM are strongly influenced by SOC, SOT, and SOH as their effects are visible under similar frequency ranges, it is difficult to custom select a few frequency points for analysis as we lose useful information from the EIS spectrum. It is advised to use all the ECM parameters and not rely on empirical relationships established between a few ECM parameters such R_2 and Q_2 which showcase a strong analytical relationship in data. Fig. 7(b) shows a zoomed pair plot of R_0 and R_1 for raw data cluster visualization as a function of SOT.

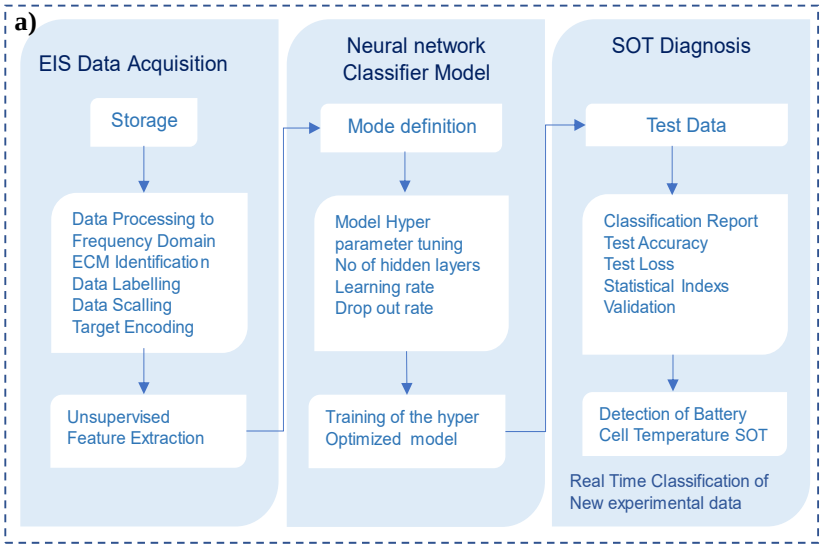

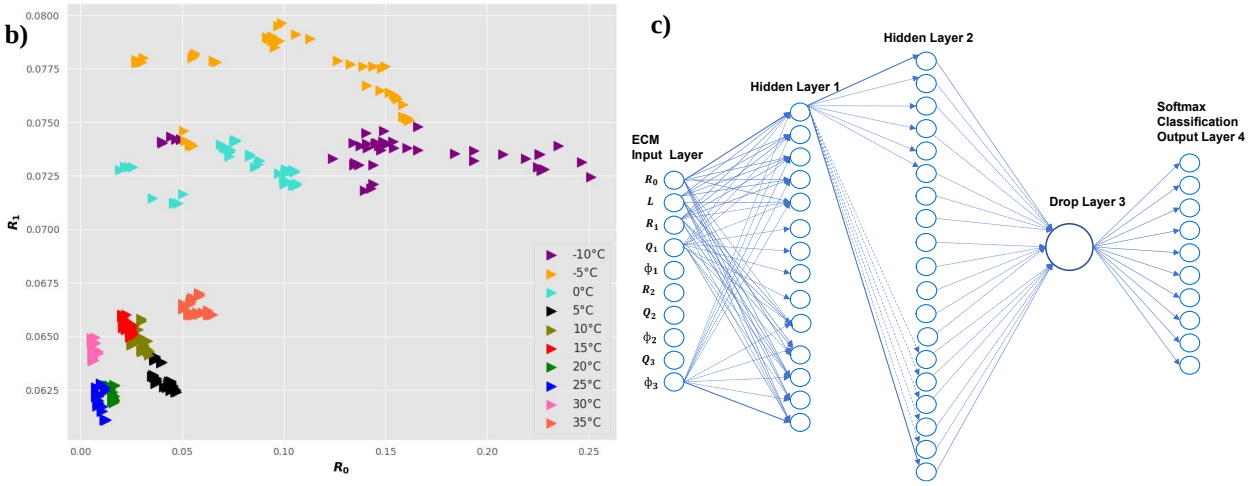

Figure 7: SOT detection by IGBM (a) classifier development methodology (b)raw input data: clusters of ECM (c) architecture of the classifier.

5.2 The Feed Forward Neural Network Classifier Model

The feedforward NNC consists of input parameters, and hidden layers with the number of neurons (function approximates) which are mapped using activating functions to adjust the weights and optimize the input to output true values. The activation function helps nonlinear mapping of input x on the output neurons at each layer. Table 7 summarizes various methods that are used in neural network modeling and their significance.

Table 7: Activation functions for deep network layers.

Activation functions	Description	Mathematical Expression	Eq. ()
Sigmoid (x)	Smooth S-curve-shaped function maps value between [0,1], best suited for binary classification problems	$F(x) = \frac{1}{1+e^{-x}}$	(19)
Hyperbolic Tangent Tanh (x)	Maps the smoothed function between [-1,1], suited for hidden layers	$F(x) = \frac{e^{2x}-1}{e^{2x}+1}$	(20)
Rectified Linear Unit ReLu (x)	The non-linear function returns 0 for -ve input values, for +ve returns input values itself, quick convergence [44] avoids the vanishing gradient problem	$F(x) = \max(0,x) = \begin{cases} 0\ (x \le 0) \\ x(x \ge 0) \end{cases}$	(21)
Leaky ReLu (x) Variant of ReLu	Prevents dead neurons for -ve input values by introducing a small slope (α) typically of 0.01	$F(x) = \max(\alpha * x, x) = \begin{cases} \alpha x\ (x \le 0) \\ x(x \ge 0) \end{cases}$	(22)
Exponential Linear Unit Variant of ReLu Elu (x)	Prevent dead neurons for -ve input, Elu's have negative values which push the mean of the activation closer to zero. It reduces the effect of gradient disappearance in complex, longer, wider, multilayered networks. [45]	$F(x) = \max(\alpha * x, x) = \begin{cases} \alpha * e^{x-1}\ (x \le 0) \\ x(x \ge 0) \end{cases}$	(23)

Since data input is nonlinear with negative temperature influence, the use of *ReLu* activation was implemented as an activation function from Eq. (21). The Fig. 7(c) represents the general architecture of a feed forward neural network classifier adapted to SOT detection by IGBM. As outlined in Fig. 7(a) various steps are implemented to optimize and hyper tune this general architecture before training the network model for its best-case preprocessed input data.

5.2.1 Data Scaling and Normalization

The key to the development of an unbiased machine learning algorithm is the generation of good-quality features. Data normalization and scaling is the preprocessing step, where the data is transformed to have specific properties that can improve the performance of the model. It allows decreasing the predominance of possible outliers and noises in the dataset and improves the robustness of the results while reducing the computation time. In NNC and various clustering techniques, such as k-means clustering, support vector machine, or k-nearest neighbors, the cluster

assignment is highly dependent on the distance calculations between data points. Hence the choice of data normalization plays a crucial role in the successful implementation of ML algorithms. The data normalization typically involves scaling the input features to have zero mean and unit variance and adjusting the data input values to the range and similar units. For example, from the input parameters of the ECM, the inductance parameter L remains significantly small 10^{-9} to 10^{-6}, while resistances R_1 and R_2 are in the range of 10^{-1} to 10^{-4}. There are three main categories to standardize the data: Normalization, Linear scaling, and Non-linear Transformation. Each method described below in the Table 8 is implemented using the scikit library [46] on the input data set and the best-performing scaler is implemented in the final network structure.

Table 8: Scaling and Normalization of Data.

Scaling-Normalizing Functions	Description	Mathematical Expression	Eq. ()
Normalizers Norm L1	Scales the data for each sample to have a unit norm $\|x\|$, independent of the distribution of the samples. Based on the Manhattan distance $\|x\|_1$, it is calculated as the sum of the absolute vector values	$f(x\_norm1) = \frac{(x)}{\|x\|_1}$ $\|x\|_1 = \|x_1\| + \|x_2\| + \cdots + \|x_N\|$	(24)
Norm L2	Based on Euclidian distance $\|x\|_2$ calculates the distance of the vector coordinates from the origin of the vector space	$f(x\_norm1) = \frac{(x)}{\|x\|_2}$ $\|x\|_2 = \sqrt{\|x_1^2\| + \|x_2^2\| + \cdots + \|x_N^2\|}$	(25)
Linear Scalers Standard scaler (x)	Scales the data to get mean $\mu_x = 0$ and a standard deviation $\sigma_x = 1$	$f(x\_scaled) = \frac{(x - \mu_x)}{\sigma_x}$	(26)
MinMaxScaler (x)	Scales the data between [0,1], by using maximum x_{max} and minimum x_{min} of x as limiting boundaries. It keeps the same distance ratio between original data points allowing smaller values compared to large ones	$f(x\_scaled) = \frac{(x - x_{min})}{(x_{max} - x_{min})}$	(27)
MaxAbosulte Scaler (x)	A variant of the MinMax scaler uses the maximum absolute value of the data x to scale it between [0,1] or [-1,1].	$f(x\_scaled) = \frac{(x)}{(max\|(x)\|)}$	(28)
Robust Scaler (x)	It removes the median (x_{median}) and scales the data according to the Inter quantile range (IQR). Advised for the data with Outliers	$f(x\_scaled) = \frac{(x - x_{median})}{(IQR)}$	(29)
Non-Linear Transformer Quantile Transformer (x)	Transforms the data so that it follows a uniform or a normal probability distribution of the data. The mapping is based on cumulative distribution function φ , and Q^{-1} Reduces the impact of outliers in the dataset	$f(x\_scaled) = (\varphi(x)) * Q^{-1}$	(30)
Power Transformer (x) Box-Cox	Transforms the data monotonically and parametrically to map the data points in Gaussian-like distribution. Box-Cox does not support negative values of the data set, (λ) power of transformation	$F(x_i^\lambda) = \begin{cases} \frac{x_i^\lambda - 1}{\lambda}, (\lambda \neq 0) \\ \ln(x_i), (\lambda = 0) \end{cases}$	(31)

5.2.2. Overfitting of the Network

Overfitting happens when the machine learning model memorizes the pattern in the training data too well and fails to classify unseen data, resulting in poor performance of the model. The noise or fluctuations in the training data are seen as features and learned by the model. This leads to the model being outperformed in the training set but poor performance in the validation and testing sets. To avoid this problem several techniques are widely implemented such as Early stopping: learning is stopped by the model if it notices an increase in validation loss, Batch Normalization: re-normalizes the inputs at each hidden layer, Bias Regularization: L1/L2 discourages the network to adapt complex patterns dependent on input features. Changing model design parameters such as number of the hidden layers, and the number of neurons at each layer influences the validation accuracy and requires retraining of the model. A simpler solution is introduced known as the Dropout Layer, where the network randomly drops a certain prefixed number of neurons in a layer which motivates the model to learn more robust and less dependent features from input data. Preventing excessing learning by certain neurons in the training process. The drop rate is represented in Eq. (32), where $a[i]$ is the output of the i^{th} neuron and p is the dropout rate. During training, each neuron in the layer has a

probability of p of being set to 0, effectively dropping out that neuron. The remaining neurons are then scaled by a factor of $\frac{1}{(1-p)}$ to maintain the expected sum of the outputs as per Eq. (33).

$$a[i] = 0, \forall\, p \tag{32}$$

$$a[i] = \frac{a[i]}{(1-p)} \tag{33}$$

5.3 Optimizing the Hyperparameters

When building a high-quality, predictive classification model, it is important to select the right features (or predictors) and tune the parameters of the model, such as the best number of neurons in each layer, rate of learning, drop rate, and kind of activation function used to minimize the error between predicted and true values. The process of finding optimized parameters to run the model at the highest accuracy without overfitting or underfitting the network is known as hyperparameter tuning. In general terms, it is an optimization problem for several Design of Experiments (DOE) to verify which experimented set of parameters yields the best results. Techniques such as Genetic algorithm, PSO, or simple grid search with predefined ranges for parameters are used to find hyperparameters but they tend to be long and computationally expensive. Li et al. [47] proposed a non-stochastic novel infinite-armed bandit-based approach that purely explores the entire search space with an aim to minimize the distance between optimal solutions.

The Hyperband optimization technique is used to optimize the model parameters of the feedforward NNC with data input from ECM parameters in a (480,11) data matrix as a function of SOC and SOT levels. The hyperband optimization of model parameters is described in the algorithm. (2). The function $get\_best\_configuration\_solution\,(\eta)$ method starts by randomly sampling a set of hyperparameter configurations using function $G(n)$ for n random configurations to evaluate. Then at each model configuration, it iterates the training and evaluation for a small number of epochs (the number of times the dataset is passed to fit the training of the model), using evaluation metrics on the validation dataset it discards the poorly performing configurations and allocates more resources to the promising ones. It performs the memory and resource allocation, where R is the maximum resources available out of which it uses only B resources evenly among n configurations by the successive-halving procedure [47] for fixed values of n and r thus reducing the computation time and costs. η, is an input that controls the proportion of configurations discarded in each round of successive halving. s_{max} is the most aggressive set of hyperparameter configurations for a tradeoff between n and $\frac{B}{n}$ resources.

Algorithm 2: Hyperband optimisation

input: R - maximum number of resources to allocate.
η - reduction factor for the number of configurations and epochs to evaluate in each round (default η = 3)

initialize: $s_{max} = (\log_{\eta} R\ )$
$B = (s_{max} + 1) * R$
for s = {s_{max}, s_{max} - 1, ..., 0} do

$n_s = \left\lceil \frac{B}{R} * \frac{\eta^s}{(s+1)} \right\rceil$
$r_s = R * \eta^{-s}$
//begin successful halving of resources (n,r)
G = get_best_configuration_solution (η)
for $i \in = \{0, \ldots., s\}$ do
$n_i = [n_s * \eta^{-i}]$
$r_i = r_s \eta^{-i}$
$L = \{run\ the\ model\ config\ , return\ its\ val_{loss}(\ g, r_i) : g \in G\}$
$G = \left\{top\_k\ (G, L, [\frac{n_i}{\eta}]\right\}$
end
end
return configuration with the smallest validation loss seen so far

The function $return\ its\ val_{loss}(\ g, r_i)$ calculate and returns the validation loss for that set of hyperparameters. While the function top_k returns the best-performing parameters. Table 9 presents the search space of hyperparameter optimization and the final optimized values obtained for the model architecture.

Table 9: Optimizing the network architecture.

Hyperparameters	Range	Step	Optimized Value
Dense hidden layer 1	1 – 64 neurons	1	52
Dense hidden layer 2	1 – 128 neurons	1	86
Drop-out layer rate	0.2 - 0.9	0.1	0.3
Learning rate	[0.01,0.001,0.0001,0.00001]	-	0.01

The final optimized architecture of the model with 52 neurons in hidden layer 1, 86 in layer 2, and a drop rate set of 0.3 at a learning rate of 0.01. The relationship between input and hidden layers of output z_I is represented by Eq. (35). Eq. (34) represents the weight matrix A_I, where W_I is the weight and $\vec{B}_I$, is the bias vector, and I is the number of layers defined in the dense sequential model.

$$(A_1) = x.*(W_1) + \vec{B}_1 \text{ , Hidden layer1} \tag{34}$$

$$(Z_1) = ReLu(A_1) \tag{35}$$

$$(A_2) = A_1.*(W_2) + \vec{B}_2 \text{ , Hidden layer2} \tag{36}$$

$$(Z_2) = ReLu(A_2) \tag{37}$$

The SoftMax layer is the output Layer 3, it is often used in the output of classification problems with multiple classes, the function maps the input to a distribution probability predicting the most probable class out of all class labels in input data indicating a value between [0 to1] and the sum of classes is always 1, the number of neurons in this layer is always same to the number of classes in true labels i.e. here for 10 classes of SOT (-10°C, -5C, 0°C, 5°C, 10°C, 15°C, 20°C, 25°C, 30°C, 35°C)

$$Softmax\ F(x_i) = \frac{e^{x_i}}{sum(e^{x_j})}, \forall\ i = \{1, \dots, N\} \tag{38}$$

$$sum\left((e^{x_j})\right) = \sum_{i=0}^{N} e^{x_i}, \forall\ i = \{1, \dots, N\} \tag{39}$$

where x_i is the output of the i^{th} neuron in the previous layer, (N) is the number of classes, and (e^x) denotes the exponential function. Integrating Eqs. (38) and (39) to predict the output of the SoftMax Layer 3 in the model we get Eqs. (40) and (41) respectively.

$$(A_3) = A_2.*(W_3) + \vec{B}_3 \text{ , Softmax layer 3} \tag{40}$$

$$(y_I) = ReLu(A_3) \text{ \% final predicted label output} \tag{41}$$

6. Prediction and Evaluation of the State of Temperature of the battery cell

The model is trained for 1500 epochs using the train method for 60% of the input scaled dataset, it is then validated on 15% of the dataset and, the last 25% is used to evaluate the network as test samples. Table 10 shows the results of the study where all the data scaling methods from Table 8 were implemented on NNC. They are compared based on the training time required, the number of epochs to reach the converging solution, and the test performance accuracy. In general, the data transformers tend to perform better than most linear scalers or normalizers. Chanal et al. [48] obtained similar results with quantile transformers outperforming other scaling methods, thus the architecture of the model is optimized and validated to retain best-performing weights and biases. From Fig. 8(a) we can see, the proposed network converges in less than the first 75 epochs in the training and with a training time of 2 min and 41 seconds on a standard runtime environment of 12 GB CPU with a testing loss of 0.09 cross-entropy error for 120 random test samples for the best performing quantile uniform scaler. The classification accuracy measures the proportion of

correctly classified samples out of the total number of samples. It is defined in Eq. (42) where *TP* -True Positives, *TN* - True Negatives, *FP*- False Positives, and *FN* -False Negatives.

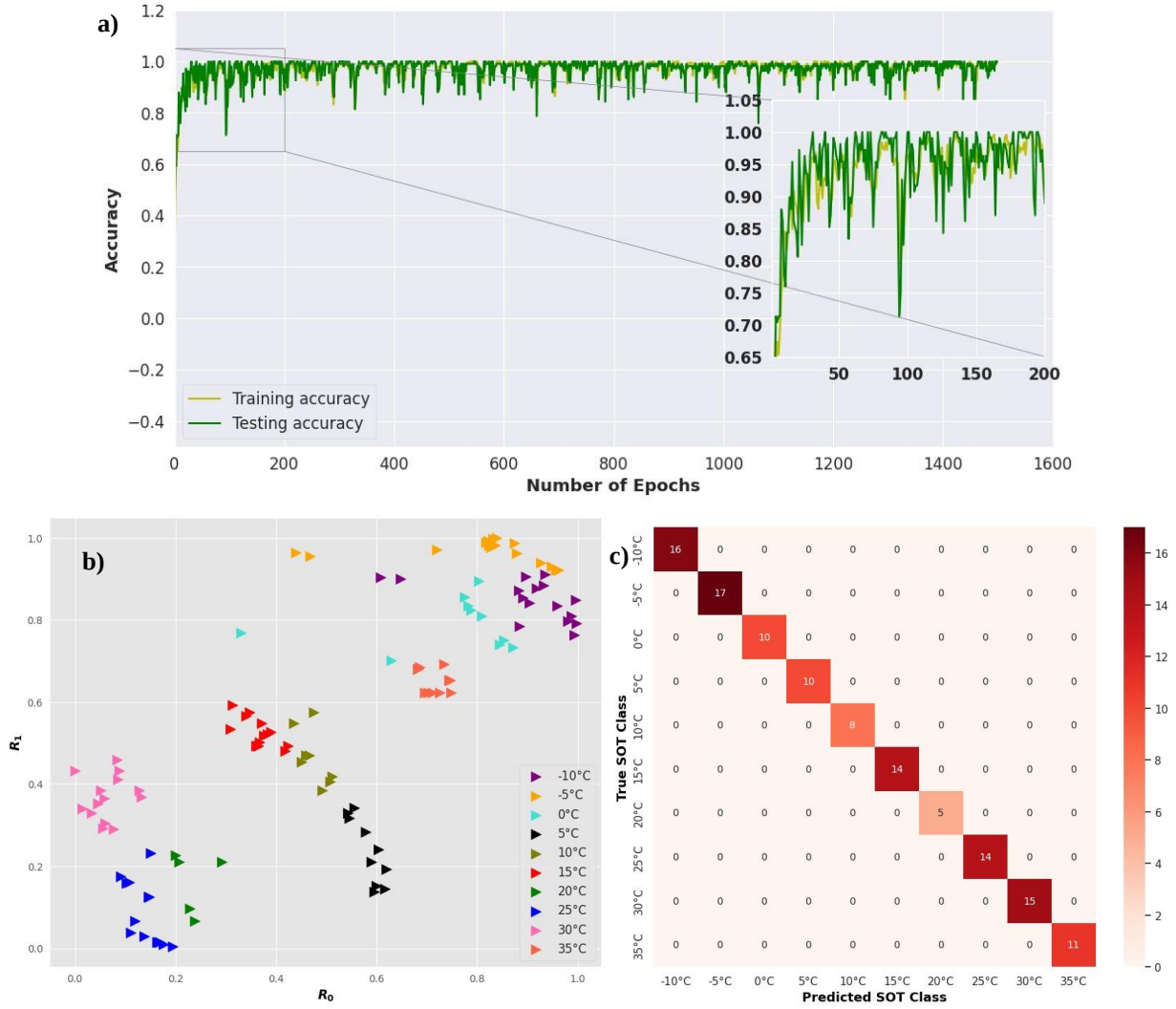

Figure 8: Classifier metrics (a)accuracy of the classifier network (b) prediction by the classifier (c) confusion matrix of the classifier.

Table 10: Effect of data scaling on classifier performance.

Scaler	Optimized Model	Training loss	Training Time min, sec	Epochs to Converge	Testing loss	Testing Accuracy	FMI
Norm L1	36,77,0.4,0.01	2.0584	2', 47.18"	9	2.186009	0.40%	0.003333333
Norm L2	63,115,0.8,0.01	2.0584	2', 47.18"	15	2.186009	12%	0.31887407
Standard	64,107,0.2,0.01	0.3557	2', 35.70"	7	0.215613	98%	0.965410242
MinMaxScaler	61,94,0.2,0.01	0.0912	2', 45.35"	66	0.079683	100%	1
MinAbsScaler	9,78,0.5,0.01	0.4084	2', 13.61"	320	0.293059	95%	0.905090265
Robust Scaler	40,114,0.4,0.01	0.3886	1',59.07"	9	0.858677	98%	0.909602696
Quantile Uniform	52,86,0.3,0.01	0.1048	2', 41.74"	55	0.09038	100%	1
Quantile Normal	16,77,0.3,0.01	0.047	2', 58.07"	23	0.110921	98%	0.96061389
Box-Cox PT	30,103,0.2,0.01	0.291877	1', 55.60"	108	0.291877	96%	0.915951207

While the Fowlkes-Mallows Index (FMI) in Eq. (43) is an evaluation metric used in clustering analysis to measure the similarity between two clustering.

$$Accuracy = \frac{(TP+TN)}{(TP+TN+FP+FN)} \quad (42)$$

$$FMI = \frac{(TP)}{\sqrt{(TP+FP)*(TP+FN)}} \tag{43}$$

The FMI ranges from 0 to 1, with a value of 1 indicating that the two clusterings are identical. A low FMI suggests that the two clusterings are dissimilar. The Fig. 8(b) represents the predictions of the test samples provided by the classifier, correctly classifying the data into each temperature group whereas Fig. 8(c) represents the confusion matrix, it provides a detailed breakdown of the model's performance by evaluating how many times the model correctly classified each sample into its appropriate true class. Generally, the diagonal matrix depicts a higher accuracy score. For every group of the true SOT class, the IGBM is able to predict with 100% accuracy and zero confusion between different sets of the SOT.

Conclusion

In this paper, a fractional order ECM model is applied to analyze the EIS of the Li-ion battery cell, and a novel state of temperature detection of cells based on an intelligent gray box model is presented. The methodology provides insight to implement the trained algorithm on the embedded system to identify the SOT of cells in a battery pack without the addition of external sensors. It can be further exploited to locate the hotspots inside the battery pack, which might eventually lead to thermal runaway or local profound degradation of the cell and the overall performance of the battery system.

The main conclusions of the article can be summarized as follows:

(1) A method to conduct EIS coherent to embedded constraints, with a detailed explanation of experimental design is presented, and its signal processing and transformation to the frequency domain is illustrated.
(2) The fractional order ECM is used to create a model of the battery considering the electro-chemical, thermal, and kinetic behavior of the battery, it corresponds well with the experimental values of EIS. The dynamic response of the battery is well captured and co-relates with the physical link between EIS and ECM. Also, the proposed hybrid parameter optimization method is found to be very efficient and robust. The 10 parameters of ECM can be identified with both a wide range and a 95% confidence interval for 480 EIS tests.
(3) The article describes in detail the architecture and implementation of optimized hyperparameters in NNC. It compares various data scaling methods, and finally, the best-performing classifier parameters are implemented in IGBM.
(4) EIS of a battery is extremely sensitive to temperature, state of charge, and aging. In this study, it is used as an indicator to identify the surface temperature of the cell, irrespective of its state of charge. Based on the relationship between estimated circuit parameters of ECM, the proposed SOT detection method by IGBM can identify with 100% accuracy of the 10 different SOT out of 120 EIS test samples.

The elevated performance of IGBM as compared to literature methods which depend solely on certain frequencies of interest is due to the fact the network is intentionally trained using ECM parameters as input features and useful information. So, it is the network learning the hidden patterns between the 10 ECM parameters, SOC% of the cell, and its associated temperature. It is far more sophisticated, robust, and precise as compared to the statistical models retaining 2-3 parameters of ECM. Another advantage of the method is that it doesn't use the voltage and current signals directly from EIS to train the network as those signals tend to be noisy which affects the performance of regular black box models. Moreover, IGBM has the potential to be applied in real-time diagnosis based on online EIS measurement, thus filling the gap between research and application for real-world use. The method can be applied to most electrochemical energy storage systems, such as fuel cells, Na, and solid-state batteries.

Acknowledgments

This work has been supported by the EIPHI Graduate School (contract ANR-17-EURE-0002) and the Region Bourgogne Franche-Comté.

References

[1] N. Lohmann, P. Weßkamp, P. Haußmann, J. M. and T. Musch, Electrochemical impedance spectroscopy for lithium-ion cells: Test equipment and procedures for aging and fast characterization in time and frequency domain, Journal of Power Source.273 (2015) 613–623. doi: https://doi.org/10.1016/j.jpowsour.2014.09.132.6.

[2] J. Christophersen, J. Morrison, W. Morrison, C. Motloch, Rapid impedance spectrum measurements for state-of-health assessment of energy storage devices, SAE Int. J. Passeng. Cars - Electron. Electr. Syst 5(1) (2012) 246–256. doi: https://doi.org/104271/2012-01-0657.

[3] Z. Yuan, H. Xiaosong, M. Hongmin, L. Shengbo, Combined state of charge and state of health estimation over lithium-ion battery cell cycle lifespan for electric vehicles, Journal of Power Sources 273 (2015) 793–803. doi: 10.1016/j.jpowsour.2014.09.146.

[4] J. Park, J. Lee, S. Kim, I. Lee, Real-time state of charge estimation for each cell of the lithium battery pack using neural networks, Applied Sciences 10 (23) (2020). doi:10.3390/app10238644.

[5] B. Liebhart, L. Komsiyska, C. Endisch, Passive impedance spectroscopy for monitoring lithium-ion battery cells during vehicle operation, Journal of Power Sources 449 (2020) 227297. doi: 10.1016/j.jpowsour.2019.227297.

[6] F. Huet, A review of impedance measurements for determination of the state-of-charge or state-of-health of secondary batteries (1 1998). doi:10.1016/S0378-7753(97)02665-7.

[7] E. Rudnicka, P. Jakobczyk, A. Lewandowski, Thermodynamic and kinetic limits of li-ion battery operation, Journal of Energy Storage 55 (2022) 105747. https://doi.org/10.1016/j.est.2022.105747.

[8] L. D. Couto, M. Kinnaert, Internal and sensor fault detection and isolation for li-ion batteries*, IFAC-Papers Online 51 (24) (2018) 1431–1438, 10th IFAC Symposium on Fault Detection, Supervision and Safety for Technical Processes SAFEPROCESS 2018. doi: https://doi.org/10.1016/j.ifacol.2018.09.536.

[9] G. Saccani, D. Locatelli, A. Tottoli, D. M. Raimondo, Model-based thermal fault detection in li-ion batteries using a set-based approach, IFAC-Papers Online 55 (6) (2022)329–334, 11th IFAC Symposium on Fault Detection, Supervision and Safety for Technical Processes SAFE PROCESS. doi: https://doi.org/10.1016/j.ifacol.2022.07.150.

[10] X. Hu, K. Zhang, K. Liu, X. Lin, S. Dey, S. Onori, Advanced fault diagnosis for lithium-ion battery systems: A review of fault mechanisms, fault features, and diagnosis procedures, IEEE Industrial Electronics Magazine 14(3) (2020) 65–91. doi:10.1109/MIE.2020.2964814.

[11] K. M. Carthy, H. Gullapalli, T. Kennedy, Real-time internal temperature estimation of commercial li-ion batteries using online impedance measurements, Journal of Power Sources 519 (2022) 230786. doi: 10.1016/j.jpowsour.2021.230786.

[12] M. A. Zabara, G. Katırcı, B. Ülgüt, Operando investigations of the interfacial electrochemical kinetics of metallic lithium anodes via temperature-dependent electrochemical impedance spectroscopy, The Journal of Physical Chemistry C 126 (2022) 10968–10976. doi: 10.1021/acs.jpcc.2c02396.

[13] G. L. Plett, Extended Kalman filtering for battery management systems of LiPB-based HEV battery packs: Part 3. State and parameter estimation, Journal of Power Sources 134 (2) (2004) 277–292. doi.org/10.1016/j.jpowsour.2004.02.033.

[14] U. Westerhoff, K. Kurbach, F. Lienesch, M. Kurrat, Analysis of lithium-ion battery models based on electrochemical impedance spectroscopy, Energy Technology 4 (2016) 1620–1630. doi:10.1002/ente.201600154.

[15] Q. Gao, H. Dai, Wei, X, and Bo. Jiang, "Impedance Modeling and Aging Research of the Lithium-Ion Batteries Using the EIS Technique," SAE Technical Paper 2019-01-0596, 2019, https://doi.org/10.4271/2019-01-0596.

[16] K. Jonghyeon, K. Lars, K. Julia, Online state-of-health estimation of lithium-ion battery cells using frequency excitation, Journal of Energy Storage 32 (2020) 101841. doi: https://doi.org/10.1016/j.est.2020.101841.

[17] C. Semeraro, M. Caggiano, A. G. Olabi, M. Dassisti, Battery monitoring and prognostics optimization techniques: Challenges and opportunities, Energy 255 (2022) 124538 https://doi.org/10.1016/j.energy.2022.124538.
[18] Y. Zhi, H. Wang, L. Wang, A state of health estimation method for electric vehicle li-ion batteries using GA-PSO-SVR, Complex Intelligent Systems 8 (2022) 2167–2182.doi:10.1007/s40747-021-00639-9.
[19] J. P. Tian, R. Xiong, W. X. Shen, F. C. Sun, Fractional order battery modeling methodologies for electric vehicle applications: Recent advances and perspectives, Science China Technological Sciences 63 (2020) 2211–2230. doi:10.1007/s11431-020-1654-0.
[20] H. Zappen, F. Ringbeck, D. U. Sauer, Application of time-resolved multi-sine impedance spectroscopy for lithium-ion battery characterization, Batteries 4 (12 2018).doi:10.3390/batteries4040064.
[21] J. Kuchly, A. Goussian, M. Merveillaut, I. Baghdadi, S. Franger, D. Nelson-Gruel, C. Nouillant, Y. Chamaillard, Li-ion battery soc estimation method using a neural network trained with data generated by a P2d model, IFAC-Papers Online 54 (2021)336–343.doi:10.1016/j.ifacol.2021.10.185.
[22] P. Vyroubal, T. Kazda, Equivalent circuit model parameters extraction for lithium-ion batteries using electrochemical impedance spectroscopy, Journal of Energy Storage 15(2018) 23–31.doi: 10.1016/j.est.2017.10.019.
[23] X. Wang, X. Wei, J. Zhu, H. Dai, Y. Zheng, X. Xu, Q. Chen, A review of modeling, acquisition, and application of lithium-ion battery impedance for onboard battery management, eTransportation 7 (2021) 100093. doi: https://doi.org/10.1016/j.etran.2020.100093.
[24] B. Jiang, D. Haifeng, Z. Jiangong, A novel battery impedance model considering internal temperature gradient, SAE Technical Papers 2018-April (2018). doi:10.4271/2018-01-0436.
[25] Q. Zhang, D. Wang, B. Yang, H. Dong, C. Zhu, Z. Hao, An electrochemical impedance model of lithium-ion battery for electric vehicle application, Journal of Energy Storage 50 (2022) 104182. doi: https://doi.org/10.1016/j.est.2022.104182.
[26] J. Zhu, Z. Sun, X. Wei, H. Dai, A new lithium-ion battery internal temperature online estimate method based on electrochemical impedance spectroscopy measurement, Journal of Power Sources 274 (2015) 990–1004.doi: https://doi.org/10.1016/j.jpowsour.2014.10.182.
[27] S. Barcellona, L. Piegari, Integrated electro-thermal model for pouch lithium-ion batteries, Mathematics, and Computers in Simulation 183 (2021) 5–19. doi: 10.1016/j.matcom.2020.03.010.
[28] Z. Li, Y. Yang, L. Li, D. Wang, A weighted Pearson correlation coefficient based multi fault comprehensive diagnosis for battery circuits, Journal of Energy Storage 60 (2023)106584. doi: https://doi.org/10.1016/j.est.2022.106584.
[29] J. Zhang, X.-G. Yang, F. Sun, Z. Wang, C.-Y. Wang, An online heat generation estimation method for lithium-ion batteries using dual-temperature measurements, Applied Energy 272 (2020) 115262. doi: https://doi.org/10.1016/j.apenergy.2020.115262.
[30] S. Jan Philipp, A. Stefan, L. André, W. Daniel, W. Thomas, I. Ellen, Measurement of the internal cell temperature via impedance: Evaluation and application of a new method, Journal of Power Sources 243 (2013) 110–117. doi: 10.1016/j.jpowsour.2013.06.013.
[31] N. Damay, K. Mergo Mbeya, G. Friedrich, C. Forgez, Separation of the charge transfers and solid electrolyte interphase contributions to a battery voltage by modeling their non-linearities regarding current and temperature, Journal of Power Sources 516 (2021)230617.doi:https://doi.org/10.1016/j.jpowsour.2021.230617.
[32] Y. Inui, S. Hirayama, T. Tanaka, Temperature dependence of impedance spectrum of charge-transfer processes in lithium-ion batteries with nickel-manganese-cobalt cathode and graphite anode, Journal of Energy Storage 44 (2021) 103390. doi: https://doi.org/10.1016/j.est.2021.103390.
[33] D. Yang, Y. Wang, R. Pan, R. Chen, Z. Chen, A neural network-based state-of-health estimation of lithium-ion battery in electric vehicles, Energy Procedia 105 (2017) 2059–2064, 8th International Conference on Applied Energy, ICAE2016, 8-11 October 2016, Beijing, China. doi: https://doi.org/10.1016/j.egypro.2017.03.583.

[34] Z. Tong, J. Miao, J. Mao, Z. Wang, Y. Lu, Prediction of li-ion battery capacity degradation considering polarization recovery with a hybrid ensemble learning model, Energy Storage Materials 50 (2022) 533–542. https://doi.org/10.1016/j.ensm.2022.05.026.

[35] M. Ma, X. Li, W. Gao, J. Sun, Q. Wang, C. Mi, Multi-fault diagnosis for series-connected lithium-ion battery pack with a reconstruction-based contribution based on parallel PCA-KPCA, Applied Energy 324 (2022) 119678. doi: https://doi.org/10.1016/j.apenergy.2022.119678.

[36] D. Andre, M. Meiler, K. Steiner, C. Wimmer, T. Soczka-Guth, S. Dirk, Characterization of high-power lithium-ion batteries by electrochemical impedance spectroscopy. I. Experimental investigation, Journal of Power Sources 196 (12) (2011) 5334–5341. doi: https://doi.org/10.1016/j.jpowsour.2010.12.102.

[37] S. Lee, Y. Kim, Samsung SDI Co., Ltd. Energy Business Division, Specification of the product: Lithium-ion Rechargeable Cell ICR18650-26F, Nov 2009, Version 1.0. Retrieved from https://docs.rs-online.com/aaf3/0900766b815d2388.pdf.

[38] M. Oldenburger, B. Bedürftig, A. Gruhle, F. Grimsmann, E. Richter, R. Findeisen, A. Hintennach, Investigation of the low-frequency warburg impedance of li-ion cells by frequency domain measurements, Journal of Energy Storage 21 (2019) 272–280.doi: https://doi.org/10.1016/j.est.2018.11.029.

[39] J. Mainka, W. Gao, N. He, J. Dillet, O. Lottin, A general equivalent electrical circuit model for the characterization of mxene/graphene oxide hybrid-fiber supercapacitors by electrochemical impedance spectroscopy impact of fiber length, Electrochimica Acta404 (2022)139740 doi: 10.1016/j.electacta.2021.139740.

[40] D. Depernet, O. Ba, A. Berthon, Online impedance spectroscopy of lead acid batteries for storage management of a standalone power plant, Journal of Power Sources 219(2012) 65–74. doi: 10.1016/j.jpowsour.2012.07.053.

[41] Y. Ao, S. Laghrouche, D. Depernet, Diagnosis of proton exchange membrane fuel cell system based on adaptive neural fuzzy inference system and electrochemical impedance spectroscopy, Energy Conversion and Management 256(2022) 115391. doi: https://doi.org/10.1016/j.enconman.2022.115391.

[42] S. Mirjalili, A. Lewis, The whale optimization algorithm, Advances in Engineering Software 95 (2016) 51–67. doi: https://doi.org/10.1016/j.advengsoft.2016.01.008.

[43] C. R. Birkl, M. R. Roberts, E. McTurk, P. G. Bruce, D. A. Howey, Degradation diagnostics for lithium-ion cells, Journal of Power Sources 341 (2017) 373–386. doi.org/10.1016/j.jpowsour.2016.12.011.14.

[44] Li D, Yang D, Li L, Wang L, Wang K. Electrochemical Impedance Spectroscopy Based on the State of Health Estimation for Lithium-Ion Batteries. Energies. 2022; 15(18):6665. https://doi.org/10.3390/en15186665.

[45] D.A. Clevert, T. Unterthiner, S. Hochreiter, Fast and accurate deep network learning by exponential linear units (ELUs) (2016). arXiv:1511.07289. https://doi.org/10.48550/arXiv.1511.07289.

[46] F. Pedregosa, G. Varoquaux, A. Gramfort, V. Michel, B. Thirion, O. Grisel, M. Blondel, P. Prettenhofer, R. Weiss, V. Dubourg, J. Vanderplas, A. Passos, D. Cournapeau, M. Brucher, M. Perrot, E. Duchesnay, G. Louppe, Scikit-learn: Machine learning in python, Journal of Machine Learning Research 12 (01 2012), doi.org/10.48550/arXiv.1201.0490.

[47] L. Li, K. Jamieson, G. DeSalvo, A. Rostamizadeh, A. Talwalkar, Hyperband: A novel bandit-based approach to hyperparameter optimization, Journal of Machine Learning Research 18 (185) (2018) 1–52. URL http://jmlr.org/papers/v18/16-558.html.

[48] D. Chanal, N. Y. Steiner, D. Chamagne, M.-C. Pera, Impact of standardization applied to the diagnosis of LT-PEMFC by fuzzy c-means clustering, in 2021 IEEE Vehicle Power and Propulsion Conference (VPPC), 2021, pp. 1–6. doi:10.1109/VPPC53923.2021.9699234.